Lawrence Berkeley National Laboratory
Recent Work

Title
Mechanistic Evidence for Ligand-Centered Electrocatalytic Oxygen Reduction with the Conductive MOF Ni3(hexaiminotriphenylene)2

Permalink
https://escholarship.org/uc/item/8fr4t6mt

Journal
ACS Catalysis, 7(11)

Authors
Miner, EM
Gul, S
Ricke, ND
et al.

Publication Date
2017-11-03

DOI
10.1021/acscatal.7b02647

License
CC BY-NC-SA 4.0

Peer reviewed

Mechanistic Evidence for Ligand-Centered Electrocatalytic Oxygen Reduction with the Conductive MOF Ni₃(hexaiminotriphenylene)₂

Elise M. Miner,[†] Sheraz Gul,[‡] Nathan D. Ricke,[†] Ernest Pastor,[‡] Junko Yano,[‡][iD] Vittal K. Yachandra,[‡] Troy Van Voorhis,[†] and Mircea Dincă*,[†][iD]

[†]Department of Chemistry, Massachusetts Institute of Technology, Cambridge, Massachusetts 02139, United States

[‡]Molecular Biophysics & Integrated Bioimaging Division, Lawrence Berkeley National Laboratory, Berkeley, California 94720, United States

S *Supporting Information*

ABSTRACT: Establishing catalytic structure−function relationships introduces the ability to optimize the catalyst structure for enhanced activity, selectivity, and durability against reaction conditions and prolonged catalysis. Here we present experimental and computational data elucidating the mechanism for the O_2 reduction reaction with a conductive nickel-based metal−organic framework (MOF). Elucidation of the O_2 reduction electrokinetics, understanding the role of the extended MOF structure in providing catalytic activity, observation of how the redox activity and pK_a of the organic ligand influences catalysis, and identification of the catalyst active site yield a detailed O_2 reduction mechanism where the ligand, rather than the metal, plays a central role. More generally, familiarization with how the structural and electronic properties of the MOF influence reactivity may provide deeper insight into the mechanisms by which less structurally defined nonplatinum group metal electrocatalysts reduce O_2.

KEYWORDS: *O_2 reduction, electrocatalysis, metal−organic framework, porous catalysts, 2D materials*
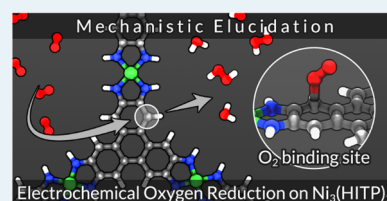
INTRODUCTION

Understanding catalytic kinetics and thermodynamics to construct a reasonable reaction mechanism is central for both elucidating the behavior of a given catalyst and gaining predictive power over structure−function relationships. This predictive power aids in efficiently optimizing catalyst performance by systematically tuning the structural and electronic properties of the catalyst. One class of materials that could benefit from mechanism-guided optimization is nonplatinum group metal (non-PGM) electrocatalysts for the O_2 reduction reaction (ORR) to water ($4e^-$ reduction) and/or hydrogen peroxide ($2e^-$ reduction). Such catalysts typically include abundant transition metals and/or heteroatoms such as N, O, and S doped into a carbonaceous matrix.[1−6] Although quite active and stable during ORR, previously reported non-PGM catalysts often consist of amorphous carbon mechanically blended with transition metal macrocycles or other metal and main group heteroatomic sources. These relatively poorly defined materials do not lend themselves to facile mechanistic studies; the inhomogeneous dispersion and irregular orientation of the dopants throughout the carbon matrix engenders structural ambiguity that makes identification, experimental probing, and computational modeling of active sites difficult.

Conversely, highly ordered metal−organic frameworks (MOFs) containing well-defined, spatially isolated active sites present an attractive platform for experimental and computational correlation between the chemical and electronic structure of a given catalyst and the electrocatalytic activity and mechanism, a feat that is traditionally restricted to homoge-
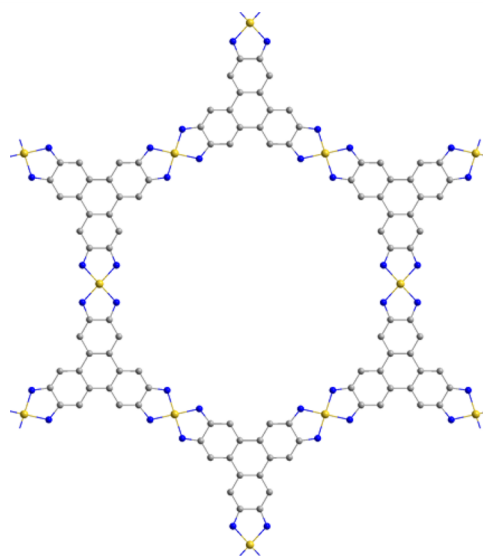

Figure 1. Ni₃(HITP)₂ structure. Ni, N, and C atoms are shown in yellow, blue, and gray, respectively. H atoms are omitted for clarity.

neous molecular systems. We previously showed that the electrically conductive MOF Ni₃(HITP)₂ (HITP = 2,3,6,7,10,11-hexaiminotriphenylene) (Figure 1) functions as

an active ORR electrocatalyst stable in alkaline medium.[7] The activity of $Ni_3(HITP)_2$ compares well with those of the most active non-PGM electrocatalysts,[1−6] with an ORR onset potential ($j = -50~\mu A \cdot cm^{-2}$) of 0.82 V versus RHE.

Unlike other non-PGM catalysts, $Ni_3(HITP)_2$ presents a well-defined structure and thus the opportunity to determine whether the ORR activity is associated with the organic building blocks or the metal ions. These results could have implications for understanding the wider class of non-PGM catalysts, whose mechanism for ORR activity remains the subject of numerous studies.

Here, we present experimental and computational evidence for a ligand-based active site in $Ni_3(HITP)_2$. Our data show no evidence for Ni involvement in the catalytic cycle, but suggest important consequences for changing the electronic structure of the ligand. Establishment of precise structure−function relationships in this material introduces the possibility for tuning the structure with atomic precision such that catalytic ORR activity, selectivity, and stability can be maximized.

RESULTS AND DISCUSSION

Having previously shown that $Ni_3(HITP)_2$ reduces O_2 electrocatalytically in strongly basic medium (0.1 M KOH), we explored its utility over the wider aqueous pH range and found that the material is competent for ORR catalysis under all alkaline conditions (pH 8 and above), but not in acidic medium. Indeed, cyclic voltammograms (CVs) of $Ni_3(HITP)_2$ above pH 8 showed catalytic waves with no loss in current density over 20 cycles, whereas catalytic current decreased with every cycle in acidic media (Figure 2).
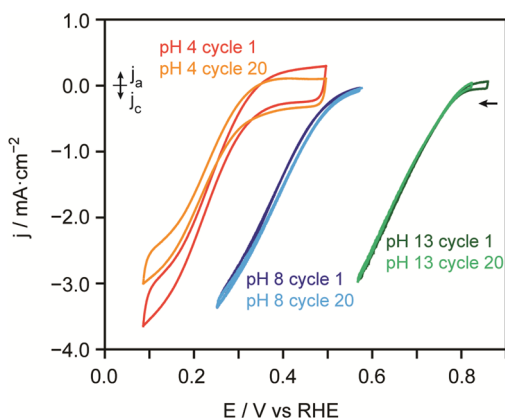

Figure 2. Cyclic voltammograms of $Ni_3(HITP)_2$ under O_2 atmosphere in pH 13, pH 8, and pH 4. Potentials are referenced versus RHE.

To derive a kinetic rate law for ORR with $Ni_3(HITP)_2$, we sought to determine the reaction order in $[O_2]$, $[H^+]$, and the number of electrons transferred prior to or during the rate-limiting step. The reaction order in $[O_2]$ was measured at varying potentials as well as varying concentrations of O_2. At pH 13, in the potential range of 0.667 to 0.787 V versus RHE, O_2 reduction exhibits an $[O_2]$ order of 0.78−0.88, nearing first-order (Figure S1a) At pH 8, in the potential range of 0.320 to 0.520 V vs RHE, O_2 reduction is also first-order in $[O_2]$ (Figure S1b).

To determine the number of electrons involved in the rate law, we collected potentiostatic data under O_2 atmosphere on a rotating disk electrode at varying rotation speeds (Figure S2), which allowed us to determine activation-controlled Tafel
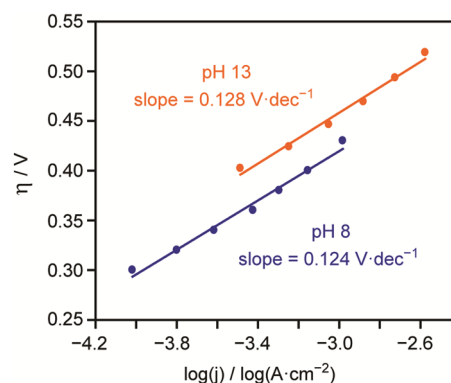

Figure 3. Tafel plots for ORR on $Ni_3(HITP)_2$ in pH 13 versus pH 8 electrolyte.

slopes. The Tafel slopes are nearly identical at pH 13 and pH 8, $-128~mV \cdot dec^{-1}$ and $-124~mV \cdot dec^{-1}$ (Figure 3), respectively, and are close to $-118~mV \cdot dec^{-1}$, the value expected for an irreversible $1e^-$ transfer in the rate-limiting step.[8] The linear Tafel slopes and consistent first-order with respect to $[O_2]$ over the activation-controlled ORR potential range suggests that the kinetic rate law does not change over the probed potential range.

To establish whether the $1e^-$ transfer step is coupled to proton transfer, galvanostatic $[H^+]$ order data was collected while titrating the alkaline electrolyte from pH 13.0 to pH 9.5 and passing a cathodic current of 10 μA in the presence of O_2. These conditions evidenced a sub-Nernstian $\delta E/\delta pH$ relationship of $-22~mV \cdot dec^{-1}$, corresponding to a fractional order of $[H^+]^{1/6}$. This low fractional order implies that there are no proton-coupled electron transfer (PCET) steps prior to or in the rate-limiting step. Although intriguing, a sub-Nernstian order in a given reactant is not unprecedented,[9−11] and can be associated with experimental conditions deviating from the ideal standards employed in electrokinetic derivations or from competing reaction kinetics, for instance. Notwithstanding, the fractional order in $[H^+]$ observed here is not caused by extraneous factors such as uncompensated Ohmic losses caused by ionic strength differences in the electrolyte: titrating toward acidic or toward basic pH values produced similar data under both O_2 and N_2 atmosphere (Figures 4 and S3). Another potential source of the fractional $[H^+]$ order is the variation of electrical conductivity of the catalyst with pH, which would lead
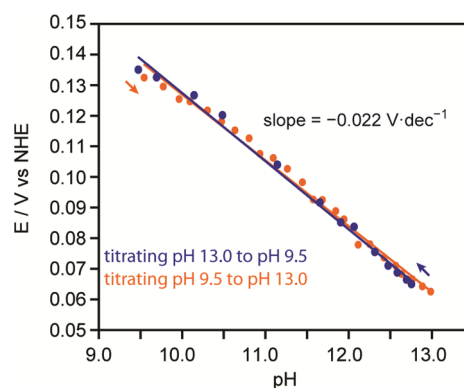

Figure 4. Dependence of ORR onset potential on pH, with acid and base titrant to show reversibility of the ORR potential dependence on pH.

to different apparent current density as a function of pH at a fixed potential. However, the electrical conductivity of $Ni_3(HITP)_2$ films grown onto interdigitated electrodes decreased with decreasing pH, a trend opposite to what would be expected if the conductivity had any effect on the kinetic rate law (Figure S4, Supplementary Note 1).

Altogether, the data above point to the following empirical rate law:

$$j = k_0 [O_2][H^+]^{1/6} e^{\alpha EF/RT}$$

where j is the measured steady state current density, k_0 is a potential-independent rate constant, E is the applied potential, α is the experimental transfer coefficient for the reaction (here, approximated as 0.5),[8,12] F is Faraday's constant, R is the gas constant, and T is the absolute temperature.

The first-order in $[O_2]$, partial order in $[H^+]$, and $1e^-$ transfer in the rate-limiting step point to O_2 binding to the catalyst as the rate-limiting step, with formation of superoxide. To identify the specific site for O_2 activation in our catalyst, we subjected films of $Ni_3(HITP)_2$ grown on indium−tin-oxide (ITO)-coated polyethylene terephthalate (PET) to in situ investigation by X-ray absorption spectroscopy (XAS) at the Ni K-edge. Potentiostatic ORR experiments on the $Ni_3(HITP)_2$ films evidenced no shift in the Ni K-edge in the X-ray absorption near-edge spectroscopic (XANES) region (Figure 5a). Additionally, the rising edge energy (8343.7 eV, measured at the half-height of the absorption edge) was close to that of a standard Ni(II) complex, nickel(II) phthalocyanine (8344.1 eV). This confirmed that Ni remains in the +2 oxidation state throughout catalysis. Furthermore, R-space extended X-ray absorption fine structure (EXAFS) spectra of $Ni_3(HITP)_2$ before and during ORR indicated no significant change in the

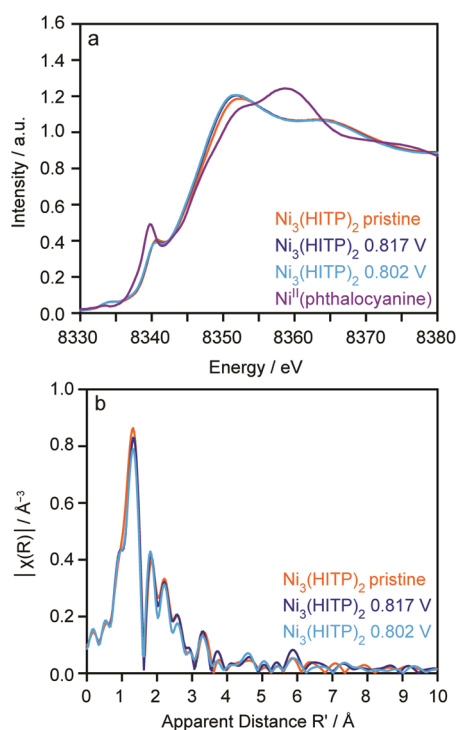**Figure 5.** (a) XANES spectrum of $Ni_3(HITP)_2$ before versus during ORR in pH 13 along with that of Ni(II) phthalocyanine; (b) Fourier transforms of k^2-weighted Ni K-edge EXAFS data of as-prepared $Ni_3(HITP)_2$ and under ORR conditions.

coordination environment or nearest neighbor distances with respect to the Ni atoms (Figure 5b). EXAFS spectra both before and during catalysis yielded similar best fit parameters giving identical Ni−N bond distances of 1.84 Å (Table S3), consistent with square-planar divalent Ni atoms.[13]

The kinetic and XAS data suggest that O_2 binding and activation in $Ni_3(HITP)_2$ do not occur on Ni, but on the ligand. To determine which of the ligand atoms present the most favorable binding site for O_2, we employed density functional theory (DFT) calculations.[14,15] Specifically, we considered a neutral fragment consisting of a central $HITP^{3-}$ ligand bound to three Ni atoms and terminated with o-diiminobenzosemiquinonate ligands (Figure 6a, Supplementary Note 2). To identify the
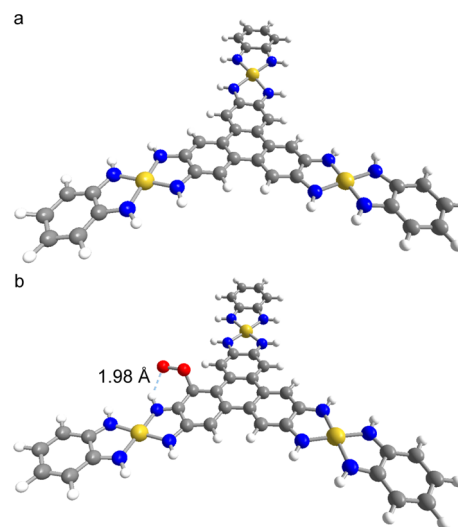

Figure 6. (a) Model fragment of $Ni_3(HITP)_2$; (b) Calculated binding site of O_2 onto the $Ni_3(HITP)_2$ fragment. C, H, N, Ni, and O atoms shown in gray, white, blue, yellow, and red, respectively.

most likely active site for catalysis, we considered specific sites where O_2 would most readily bind: the Ni atom, the imine N atoms, or one of the three unique C atoms. The calculations indicated that chemical binding of O_2 to the Ni center had an uphill free energy of 1.4 eV, and no energy minimum was found for binding O_2 to a nitrogen atom, which together pointed to a carbon-based active site. Of the three unique C atoms, the optimal binding site was calculated to be the β-C relative to the imine group, as shown in Figure 6b. Although the binding energy of O_2 to this C atom in the absence of electron transfer was found to be uphill by 1.1 eV, no energy minimum was found for the remaining two distinct C sites, which are therefore unfavorable for O_2 binding.

The potential for this β-C atom to serve as an O_2 binding site was further supported by Mulliken charge population analysis.[16] Whereas all other atoms had Mulliken populations of close to zero, the β-C was found to have a Mulliken population of −1.01 (Figure S5). This larger population indicates a likely site for reactivity, as charge localization can point to the easiest location for breaking aromaticity. Importantly, the orientation of the C-bound O_2 with respect to the NH group of the HITP ligand raises the possibility of a stabilizing hydrogen bonding interaction between the distal O atom and the imine proton, which indeed were found to lie 1.98 Å apart.

Given that the thermodynamic barrier for O_2 binding to the optimal carbon site was still higher than would be expected given the observed catalytic activity, we investigated the

possibility of electron transfer accompanying O$_2$ binding. Indeed, binding of O$_2$ to the Ni$_3$(HITP)$_2$ fragment in concert with a 1e$^-$ transfer to O$_2$ to form superoxide was found to be endergonic by only 0.1 eV in the absence of an applied potential. Notably, the barrier for electrochemical binding of O$_2$ to the Ni sites was found to be considerably higher, at 0.6 eV. The barrier for electrochemical binding of O$_2$ to the β-C is not prohibitive and is consistent with the experimental observation of first order [O$_2$] dependence as well as a Tafel slope of approximately -118 mV·dec^{-1}.[8] In agreement with rate-limiting superoxide formation, subsequent protonation of superoxide was calculated to be exergonic by 0.3 eV. Lastly, our calculations indicate that transfer of a second electron to break the oxygen-catalyst bond and release H$_2$O$^-$ is favorable by 1.2 eV (Figure 7, Table S4). Although Ni serving as an O$_2$
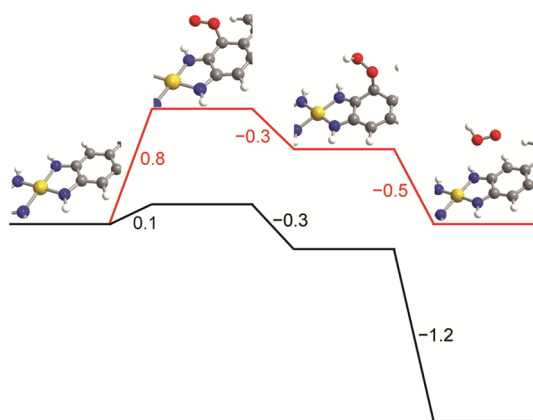

Figure 7. Free energy (eV) of each intermediate in the 2e$^-$ ORR catalytic cycle with Ni$_3$(HITP)$_2$. The lower states (black) show the energetics at open circuit potential, whereas the upper states (red) show the free energy of each state with 0.69 V versus RHE applied potential such that the production of HO$_2^-$ is thermodynamically reversible.

binding site here is unlikely, the spin-density plot of the MOF model fragment shows that electrochemical binding of O$_2$ breaks the spin symmetry, with excess spin distributed across both the metal and ligand (Figure S6). Thus, the Ni sites do not directly participate in O$_2$ reactivity, but they do contribute to the electronic structure of the ORR-active species.

To obtain a more comprehensive picture of the full catalytic mechanism, potential sources of the fractional order in [H$^+$] were further investigated. The earlier discussion on this subject notwithstanding, a plausible explanation for the partial proton order is that the absolute rate of the rate-limiting step—here, formation of MOF-bound superoxide—is only marginally slower than a subsequent proton-dependent non-rate-limiting step.[12] Such a scenario would be consistent with a pH-dependent electron transfer from Ni$_3$(HITP)$_2$ to superoxide. To probe this hypothesis, we investigated the CV signature of the catalyst under pure N$_2$ as a function of pH. As shown in Figure S7, the oxidation potentials of Ni$_3$(HITP)$_2$ are indeed pH-dependent, indicating that changing the oxidation state of Ni$_3$(HITP)$_2$ is a PCET process. More specifically, as the pH decreases, the oxidation potentials of Ni$_3$(HITP)$_2$ shift more positively with a $\delta E_{redox}/\delta pH$ slope of 90–120 mV·dec^{-1} (Figure S8), as expected for a 2H$^+$-1e$^-$ coupled transfer.[17] This Nernstian dependence of the MOF oxidation potentials on pH supports the hypothesis that the second (i.e., the non-

rate-limiting) electron transfer step is associated with proton transfer and therefore is likely responsible for the fractional [H$^+$] order during ORR. Similar pH-dependent redox activity was reported in a nitrogen-doped graphitic carbon ORR catalyst.[9]

With the discussed experimental and computational data in hand, the following mechanism for the 2e$^-$ reduction of O$_2$ on Ni$_3$(HITP)$_2$ emerges (Scheme 1):

    I. Rate-limiting electron transfer and binding of O$_2$ to the β-C with respect to the ligand imine to form the superoxide adduct

    II. Protonation of bound O$_2^-$ by water to form a hydroperoxide

    III. Electron transfer to the hydroperoxide and desorption of HO$_2^-$

    IV. Regeneration of the catalyst resting state

This proposed mechanism is consistent with our experimental data and the computational studies, but it does not address whether the highly delocalized frontier orbitals of Ni$_3$(HITP)$_2$ are necessary for catalysis or whether a smaller fragment of this material is sufficient for competent catalysis. To investigate the possibility of a small-molecule mimic of Ni$_3$(HITP)$_2$ acting as a competent ORR catalyst, we focused on the well-known molecular complex Ni(ISQ)$_2$ (ISQ = o-diiminobenzosemiquinonate, Figure 8).[18−25] Importantly, under conditions mimicking those employed for Ni$_3$(HITP)$_2$, Ni(ISQ)$_2$ showed no ORR activity (Figure S9).

Density functional theory (DFT) provided insight into the dramatic difference in catalytic activity between the MOF and the molecular complex (Figure S10). Specifically, whereas O$_2$ binding and electron transfer to the MOF is endergonic by only 0.1 eV (see above), calculations suggest that the formation of the superoxide complex with Ni(ISQ)$_2$ is endergonic by 0.7 eV at pH 13. Although in line with the experimental observation that the molecular complex is not a good ORR catalyst, this difference is surprisingly large and highlights the importance of having a delocalized valence band in the MOF. Indeed, representations of the highest occupied molecular orbitals for Ni(ISQ)$_2$ and the more extended Ni$_3$(HITP)$_2$ model system described earlier show significant redistribution of the π electron density in Ni(ISQ)$_2$, but very little disruption of the π system in Ni$_3$(HITP)$_2$ (Figure S11). In other words, the MOF is able to accommodate the key superoxide complex without significant disruption of its electronic structure, only by virtue of its extended covalent lattice. Thus, even though the metal itself does not play a significant role in ORR catalysis, the conductivity and electron delocalization in the MOF is essential for catalysis.

■ CONCLUSIONS

Electrochemical and spectroscopic techniques supported by computational evidence revealed that the active site for catalytic O$_2$ reduction with Ni$_3$(HITP)$_2$, an electrically conductive MOF, is not metal-based, as proposed for many transition-metal macrocycles, but rather ligand-based. The highly ordered MOF structure and well-defined active sites have enabled precise correlation of the structure and electronic structure of the catalyst with the ORR activity and mechanism, including the identification of a partial proton order related to the pH dependence of the MOF oxidation potentials. This comprehensive model for O$_2$ binding thermodynamics, electrokinetics, and detailed mechanism of ORR on Ni$_3$(HITP)$_2$ should enable

Scheme 1. Proposed Mechanism for 2e⁻ O₂ Electroreduction with Ni₃(HITP)₂
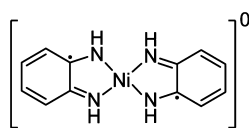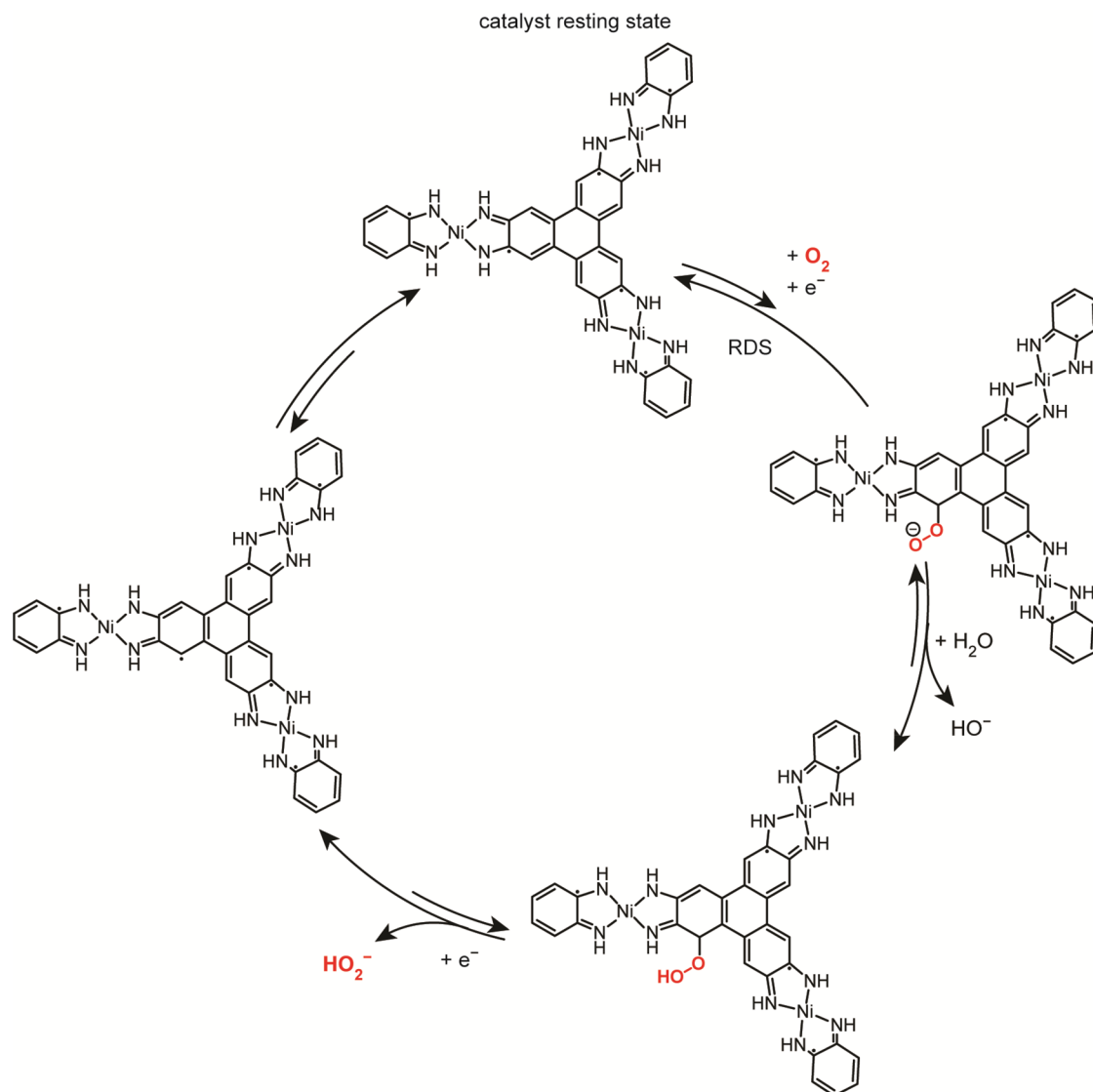
Figure 8. Structure of Ni(ISQ)₂.

catalyst design in other conductive MOF systems. Most importantly, these studies show that electron delocalization is critical for accessing key intermediates that become energetically prohibitive for molecular systems bearing only structural resemblance to the MOFs.

ASSOCIATED CONTENT

S Supporting Information

The Supporting Information is available free of charge on the ACS Publications website at DOI: 10.1021/acscatal.7b02647.

Potentiostatic ORR order in [O₂] with corresponding slopes. Koutecky−Levich data at pH 8. Current versus pH data under N₂. Dependence of electrical conductivity on pH. Mulliken charge population analysis of the Ni₃(HITP)₂ model fragment before versus after electro-

chemical O₂ binding. Excess spin density plot of superoxide bound-Ni₃(HITP)₂ model fragment. Dependence of MOF redox potentials on pH. Pourbaix diagram of Ni₃(HITP)₂. CV of Ni(ISQ)₂ under N₂ and O₂. Calculated structures for Ni(ISQ)₂ and a representative Ni₃(HITP)₂ fragment. Calculated HOMOs for Ni(ISQ)₂ and Ni₃(HITP)₂ fragment with and without bound superoxide. Best-fit parameters for Ni K-edge EXAFS curve fitting. Calculated thermodynamic data for ORR with the Ni₃(HITP)₂ fragment and Ni(ISQ)₂ (PDF)

AUTHOR INFORMATION

Corresponding Author

*E-mail: mdinca@mit.edu.

ORCID

Junko Yano: 0000-0001-6308-9071
Mircea Dincă: 0000-0002-1262-1264

Notes

The authors declare no competing financial interest.

■ ACKNOWLEDGMENTS

■ REFERENCES

(1) He, W.; Wang, Y.; Jiang, C.; Lu, L. *Chem. Soc. Rev.* **2016**, *45*, 2396−2409.

(2) Jia, Q.; Ramaswamy, N.; Tylus, U.; Strickland, K.; Li, J.; Serov, A.; Artyushkova, K.; Atanassov, P.; Anibal, J.; Gumeci, C.; Barton, S. C.; Sougrati, M.-T.; Jaouen, F.; Halevi, B.; Mukerjee, S. *Nano Energy* **2016**, *29*, 65−82.

(3) Raj, C. R.; Samanta, A.; Noh, S. H.; Mondal, S.; Okajima, T.; Ohsaka, T. *J. Mater. Chem. A* **2016**, *4*, 11156−11178.

(4) Wu, G.; Zelenay, P. *Acc. Chem. Res.* **2013**, *46*, 1878−1889.

(5) Masa, J.; Xia, W.; Muhler, M.; Schuhmann, W. *Angew. Chem., Int. Ed.* **2015**, *54*, 10102−10120.

(6) Shi, H.; Shen, Y.; He, F.; Li, Y.; Liu, A.; Liu, S.; Zhang, Y. *J. Mater. Chem. A* **2014**, *2*, 15704−15716.

(7) Miner, E. M.; Fukushima, T.; Sheberla, D.; Sun, L.; Surendranath, Y.; Dincă, M. *Nat. Commun.* **2016**, *7*, 10942−10948.

(8) Gileadi, E. *Physical Electrochemistry*; Wiley-VCH Verlag GmbH & Co. KGaA: Weinheim, 2011.

(9) Li, Q.; Noffke, B. W.; Wang, Y.; Menezes, B.; Peters, D. G.; Raghavachari, K.; Li, L. *J. Am. Chem. Soc.* **2014**, *136*, 3358−3361.

(10) Sepa, D. B.; Vojnovic, M. V.; Vracar, Lj. M.; Damjanovic, A. *Electrochim. Acta* **1987**, *32*, 129−134.

(11) Ramaswamy, N.; Mukerjee, S. *J. Phys. Chem. C* **2011**, *115*, 18015−18026.

(12) Gileadi, E. *Electrode Kinetics for Chemists, Chemical Engineers, and Materials Scientists*; Wiley, John & Sons, Incorporated: New York, 1993.

(13) Robertson, J. M.; Woodward, I. *J. Chem. Soc.* **1937**, 219−230.

(14) Kohn, W.; Sham, L. J. *Phys. Rev.* **1965**, *140*, A1133−A1138.

(15) Hohenberg, P.; Kohn, W. *Phys. Rev.* **1964**, *136*, B864−B871.

(16) Mulliken, R. S. *J. Chem. Phys.* **1955**, *23*, 1833−1840.

(17) Weinberg, D. R.; Gagliardi, C. J.; Hull, J. F.; Murphy, C. F.; Kent, C. A.; Westlake, B. C.; Paul, A.; Ess, D. H.; McCafferty, D. G.; Meyer, T. J. *Chem. Rev.* **2012**, *112*, 4016−4093.

(18) Feigl, F.; Fürth, M. *Monatsh. Chem.* **1927**, *48*, 445−450.

(19) Balch, A. L.; Holm, R. H. *J. Am. Chem. Soc.* **1966**, *88*, 5201−5209.

(20) Stiefel, E. I.; Waters, J. H.; Billig, E.; Gray, H. B. *J. Am. Chem. Soc.* **1965**, *87*, 3016−3017.

(21) Marks, D. R.; Phillips, D. J.; Redfern, J. P. *J. Chem. Soc. A* **1967**, 1464−1469.

(22) Marks, D. R.; Phillips, D. J.; Redfern, J. P. *J. Chem. Soc. A* **1968**, 2013−2017.

(23) Bachler, V.; Olbrich, G.; Neese, F.; Wieghardt, K. *Inorg. Chem.* **2002**, *41*, 4179−4193.

(24) Herebian, D.; Bothe, E.; Neese, F.; Weyhermüller, T.; Wieghardt, K. *J. Am. Chem. Soc.* **2003**, *125*, 9116−9128.

(25) Das, A.; Han, Z.; Brennessel, W. W.; Holland, P. L.; Eisenberg, R. *ACS Catal.* **2015**, *5*, 1397−1406.